Reexamining the Power-law Relationship between Global Solar X-Ray Luminosity and Total Unsigned Magnetic Flux

Keiji Yoshimura, Aki Takeda, D. W. Longcope

The Astrophysical Journal, 992:165 (11pp), 2025 October 20 https://doi.org/10.3847/1538-4357/ae0a54

Reexamining the Power-law Relationship between Global Solar X-Ray Luminosity and Total Unsigned Magnetic Flux

Keiji Yoshimura, Aki Takeda, and Dana W. Longcope
Department of Physics, Montana State University, Bozeman, MT 59717, USA; keiji.yoshimura@montana.edu
Received 2025 May 2; revised 2025 August 15; accepted 2025 September 21; published 2025 October 13

Abstract

The mechanism heating the solar corona remains unclear but is generally hypothesized to involve magnetic fields. One probe of this hypothesis is a statistical study relating coronal emission to magnetic flux. A. A. Pevtsov et al. conducted such a survey relating X-ray luminosity (L_X) to unsigned photospheric magnetic flux (Φ_m) for a variety of heated plasmas, ranging from solar quiet regions to T Tauri stars. They reported that a power-law relationship, $L_X \sim \Phi_m^{1.15}$, described the entire collection but found that the subset from solar disk–integrated flux was better fit by a broken power law. Several parameters entering the calculations of L_X and Φ_m have the potential to impact this analysis. The present study uses more recent data to reanalyze the flux–luminosity relationship for the full solar disk and examines its dependence on parameters. We find the most significant effects from two parameters: the cutoff field strength used in computation of Φ_m and the range of wavelengths defining L_X. We find further that lower choices of cutoff yield a broken power law, while an optimal choice yields a single power law and minimizes the fitting residual. The critical cutoff is well above the magnetogram noise level, suggesting that weaker fields may not contribute significantly to the X-ray corona. We also find that L_X defined by decreasing wavelength ranges requires an increasing critical cutoff. The resulting power-law indices vary, but all fall around 1.2.

Unified Astronomy Thesaurus concepts: Solar coronal heating (1989); Solar magnetic fields (1503); Solar spectral irradiance (1501)

1. Introduction

Ever since W. Grotrian (1939) and B. Edlén (1943) showed that the solar corona was composed of million-degree plasma, many scientists have tried to elucidate the heating mechanism of the outermost atmosphere (see J. A. Klimchuk 2006; F. Reale 2010; C. E. Parnell & I. De Moortel 2012; J. A. Klimchuk 2015 for reviews). Although the details of the heating mechanism are still unclear, a prevailing consensus exists among researchers regarding the critical role of the magnetic field in the process.

One of the approaches to understanding the heating mechanism is to conduct a statistical study on the relationship between coronal emission and photospheric magnetic field. For example, L. Golub et al. (1980) and S. Yashiro & K. Shibata (2001) derived a power-law relationship between the thermal energy of X-ray corona and total magnetic flux of solar active regions. G. H. Fisher et al. (1998) compared the relationship between the X-ray luminosity (L_X) and various magnetic variables of active regions on the Sun. They found that the total unsigned magnetic flux (Φ_m) is best correlated with L_X, which can be expressed $L_X \sim \Phi_m^{1.19}$. They also suggested that the coronal heating with Alfvén wave can produce the relationship, which was reproduced by a numerical simulation study (M. Shoda & S. Takasao 2021). A. A. Pevtsov et al. (2003) studied the relationship between L_X and Φ_m for 12 orders of magnitude, from the quiet region of the Sun through T Tauri stars. They found the relationship can be expressed by a single power law $L_X \sim \Phi_m^{1.15}$ for the whole range. S. Toriumi & V. S. Airapetian (2022) studied the relationship of multitemperature plasma, covering from the chromosphere through the corona by using both solar and stellar data. They found a trend that the power-law indices are smaller for the low-temperature range, but for all ranges the indices are close to unity. On the other hand, some studies using only stellar data reported larger power-law indices (A. A. Vidotto et al. 2014; O. Kochukhov et al. 2020).

The calculation of X-ray luminosity and total unsigned magnetic flux is contingent upon the selection of several critical parameters. In the present work we test the impact of parameter selection on the results, with a particular focus on the power-law indices.

A. A. Pevtsov et al. (2003) reported a broken power law resulting in a "knee" structure evident in the solar full-disk data set. This structure consists of different power-law indices in the low-magnetic-flux end (index 2) and the high end (index 1). They suggested the possibility that the existence of the coronal hole may create the knee but did not present any evidence. One of the objectives of the present study is to ascertain the nature of the "knee" and, in particular, whether it is a result of natural phenomena or an artifact. A. A. Pevtsov et al. (2003) used the data from the soft X-ray telescope on board the Yohkoh satellite and the magnetograms from the National Solar Observatory/Kitt Peak. Here we use more recent data—X-ray images from the X-Ray Telescope (XRT) on board the Hinode and magnetograms of the Helioseismic and Magnetic Imager (HMI) on board the Solar Dynamics Observatory (SDO)—to analyze L_X and Φ_m for full-Sun data.

2. Data

2.1. Hinode/XRT

The XRT (L. Golub et al. 2007; R. Kano et al. 2008) on board the Hinode satellite (T. Kosugi et al. 2007) is a grazing-incidence X-ray telescope with multiple analysis filters,

covering 1–30 MK coronal plasma. The XRT routinely takes full-disk solar images with multiple exposure time and with various filters as synoptic observation. For each filter, a set of multiple exposure images is processed into a single composite image to obtain a larger dynamic range of X-ray intensities (A. Takeda et al. 2016). This study uses these synoptic composite images as the X-ray portion of the data source. After standard calibration processes by the IDL program xrt_prep.pro, we subtracted the stray light component (A. Takeda et al. 2016) from the data and then created composite data. The exposure times of the synoptic images are optimized by a duty XRT operator. However, it is inevitable that the X-ray data contain some saturated pixels when a transient brightening or flare occurs on the Sun. We do not use such data with saturated pixels because we cannot recover the counts in them. This process removes the X-ray data with transient brightenings and makes our data set practically quiet solar data.

The total X-ray flux of each composite image is calculated by integrating the intensity of all pixels within a circle of radius R_X, centered on the solar disk. The parameter R_X was introduced to mitigate the contribution of over-the-limb corona to the X-ray luminosity, which is not associated with the observable magnetic field on the solar disk.

We selected every usable pair of X-ray fluxes from different analysis filters taken within 3 minutes of one another in order to apply the filter ratio method (G. S. Vaiana et al. 1973; N. Narukage et al. 2011). We thereby obtain a single disk-integrated plasma temperature (T_e) and emission measure (EM) for the selected portion of the solar disk.

The temperature response function of the XRT undergoes variation over time due to the degradation of the instrument. The current standard software for temperature analysis (xrt_teem.pro) implements the correction of temperature response functions by gradually increasing contamination layer on CCD over time and by the contamination layers on X-ray analysis filters developed concentratedly during the early phase of the mission (until early 2007). In this study, we add two more corrections of the temperature response functions: (1) change of prefilter's open fraction due to the fractures developed multiple times since 2013; (2) increase of contamination layer on X-ray analysis filters since 2010. The implementation of these extra corrections is still in the experimental phase but is currently considered to be the best practice to reasonably quantify the variation of T_e and EM over a solar cycle.

In order to synthesize an X-ray spectrum from the derived T_e and EM, we use two different CHIANTI models (K. P. Dere et al. 1997, 2019; G. Del Zanna et al. 2021), versions 9.1 and 10.0, with two different abundance models: "corona" (U. Feldman 1992) and "hybrid" (A. Fludra & J. T. Schmelz 1999). We use the same model for the XRT response function calculation in the above process for consistency.

The X-ray luminosity, L_X, is calculated by integrating the synthesized spectrum of an isothermal plasma with given temperature T_e over a specified wavelength range (W_X) and multiplying by the total EM. The default choice will be the wavelength range that A. A. Pevtsov et al. (2003) used in their study (2.8–36.6 Å). To understand various contributions to coronal heating we consider several other ranges as well.

The present study uses XRT data obtained until 2024 October 31 with Al-Mesh, Al-Poly, and Thin-Be filters, since they provide best coverage over the solar cycle. In the early phase of the mission, XRT synoptic observations were performed mainly using Al-Mesh and Ti-Poly filers. However, in 2015 June Ti-Poly filter became unusable due to significant contamination of visible stray light component and was replaced with Al-Poly filter. Thin-Be filter was added to the regular synoptic sequence since 2011 February in response to increasing Sun's activity level. In recent years, synoptic observation is performed at least twice per day. The total number of L_X data points is 7784 for Al-Mesh/Thin-Be combination, 6669 for Al-Poly/Thin-Be, and 6160 for Al-Mesh/Al-Poly, whose long-term variation is shown in Figure 1.

The errors in L_X are primarily due to the systematic (nonstatistical) uncertainties (A. R. Kobelski et al. 2014). They are estimated to be smaller than 3% for all data sets in this study, which are too small to affect the calculation of the power-law index. A possibly larger source of error is our assumption of uniform temperature of the whole corona. A preliminary study indicates that this assumption results in an overestimation of L_X about 10% compared to the multi-temperature calculation.

The intrinsic variability of the X-ray corona, even over relatively short times, leads to scatter that is likely to dominate any contributions from noise. To assess this contribution, we collected 57 measurements of L_X from 4 × 4 binning single exposure (noncomposite) full-Sun images observed over a 10 hr window on 2024 April 1. While the magnetic flux showed no change over this 10 hr window, L_X showed fluctuations with a 15% standard deviation around a steady mean. Although the quality of the data is not the same as those used in the main part of this study, we consider the fluctuations observed in this sample period as representing the intrinsic variation of X-ray corona, which contributes as statistical uncertainty included in the measurement of L_X at any time.

2.2. SDO/HMI

The HMI on board the SDO provides us with magnetograms of the whole Sun (P. H. Scherrer et al. 2012; J. Schou et al. 2012). We use the level 1.5 line-of-sight (LOS) magnetograms of 720 s cadence (S. Couvidat et al. 2016) for our study. The data selection was made based on the quality keyword of the FITS header. In addition, the data obtained within 2 hr after satellite's dawn were eliminated because the quality of magnetogram is low.

After the correction of projection effect by assuming the magnetic field is radial, we integrated the unsigned magnetic flux of all pixels with field strength, $|B_r|$, greater than a cutoff value (B_c). The integration was performed over a disk of radius R_m, centered on the solar disk. The foreshortening of the area corresponding to each pixel is corrected during the integration.

The parameter B_c is introduced, first, to mitigate various possible noise contributions. The issue at hand is that the magnitude of an observed value that includes noise is not an unbiased estimate of the magnitude of the underlying value. We find below that weaker photospheric field is not coupled to, or at least does not heat, the X-ray corona (see Section 4). There we show that the appropriate choice of B_c, far above the noise level, eliminates most of this weaker flux from Φ_m to reveal the underlying relationship to coronal heating.

2.3. L_X–Φ_m Plots

We select pairs of XRT and HMI data, which are taken within 1 hr of each other to make a log–log scale scatter (L_X–Φ_m) plot (see Figure 2 for examples of the plots).

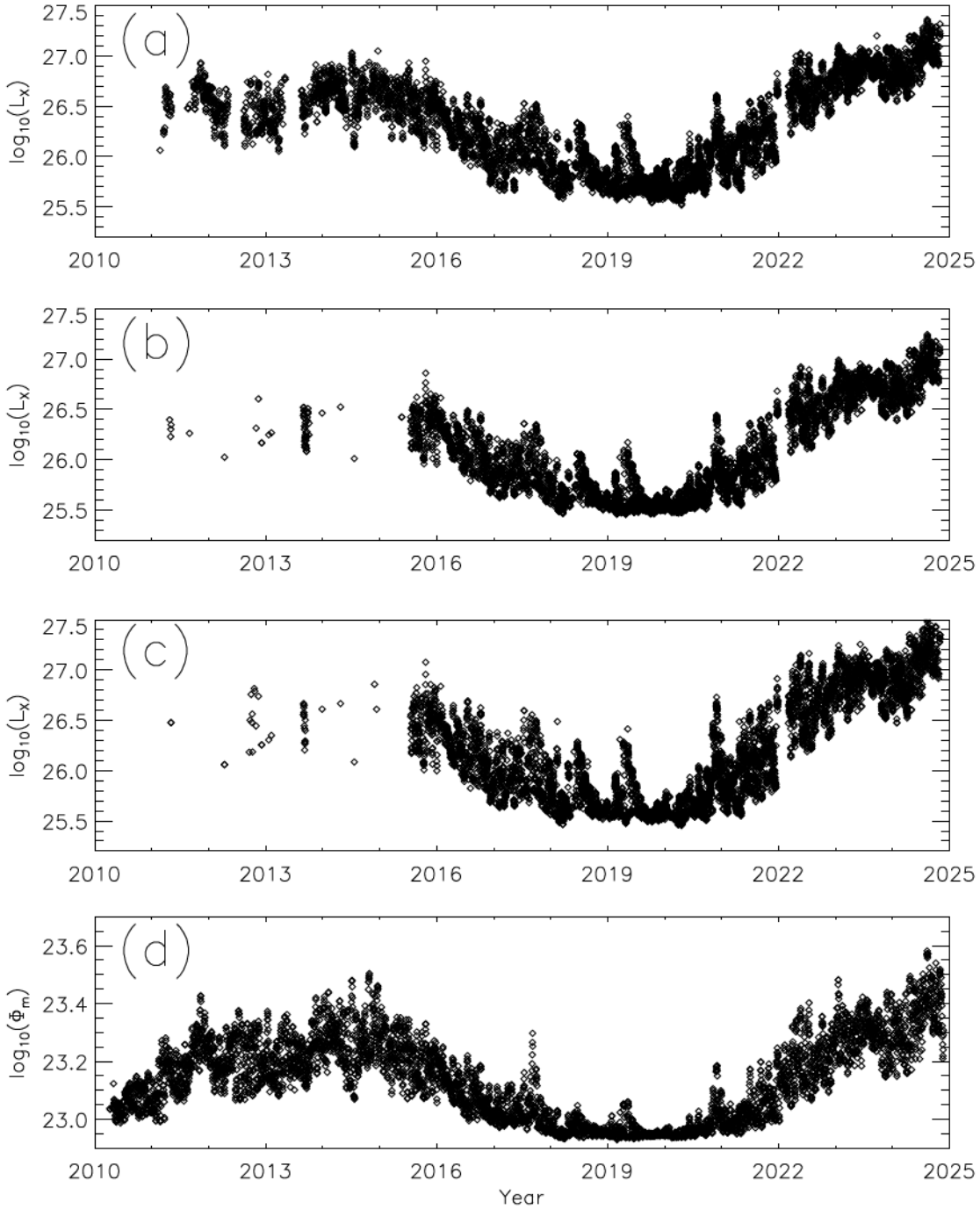

Figure 1. The time plots of the derived L_X ((a), (b), and (c)) and Φ_m (d). The L_X is calculated from the filter pairs of (a) Al-Mesh/Thin-Be, (b) Al-Poly/Thin-Be, and (c) Al-Mesh/Al-Poly.

Following previous investigations, we first perform a linear least-squares fit in log–log space to fit the plot to a single power law with index $_0$. Then, in order to address the issue of the knee, we perform a nonlinear least-squares fit in log–log space to the broken power law,

$$L(\Phi) = \begin{cases} L_* (\Phi/\Phi^*)^{\alpha_{\rm lo}}, & \Phi \leqslant \Phi_* \\ L_* (\Phi/\Phi^*)^{\alpha_{\rm hi}}, & \Phi > \Phi_*, \end{cases} \quad (1)$$

where L_*, Φ^*, $_{\rm lo}$, and $_{\rm hi}$ are parameters of the fit. We initialize the nonlinear fit with parameters matching the single power law, $_{\rm lo} = _{\rm hi} = _0$, and then vary all four parameters independently to minimize the squared residuals, $[\log_{10} L_X - \log_{10} L(\Phi_m)]^2$, summed over all data points. The additional fitting parameters (four rather than two) lead to a lower residual for the broken power law than the single power law. In some cases, however, it is not much lower.

In all of our least-squares fitting, the uncertainty in the parameters is calculated under the assumption that the true distribution really does match the model and that scatter is due to the measurement uncertainty (see W. H. Press et al. 1992, Section 15.2 for details). The measurement uncertainties are 0.04 for $\log_{10}(\Phi_m)$ and 0.05 for $\log_{10}(L_X)$ in the case of Figure 2(d). This permits us to compute uncertainties $_0$, $_{\rm lo}$, and $_{\rm hi}$.

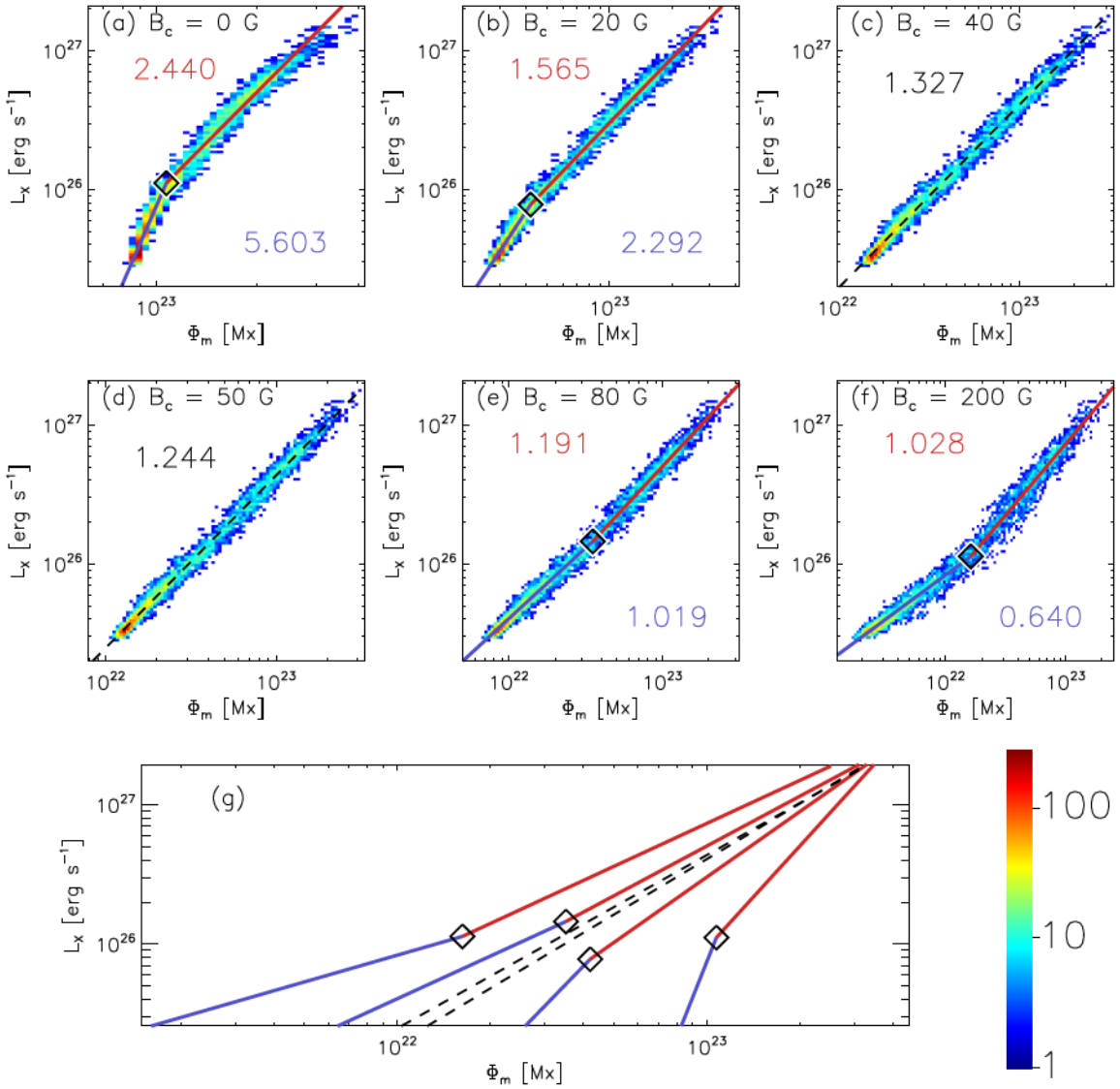

Figure 2. Two-dimensional histograms in Φ_m–L_X space using W_X = 2.8–36.6 Å, XRT filter pairs Al-Poly and Thin-Be, B_c = (a) 0, (b) 20, (c) 40, (d) 50, (e) 80, and (f) 200 G. The fitted lines are plotted in red (high end) and blue (low end) for broken power-law distribution. Each power-law index is displayed in red (high end), blue (low end), and black (single power law). The common color bar for the histograms is shown at the bottom-right corner of the figure. All fitted broken and single power-law lines are plotted in one graph in (g).

3. Results

This study investigates the L_X versus Φ_m relation for multiple parameters of considerable range. To describe the impact of each parameter selectively, we designate the default values of these parameters, as listed in Table 1. We explain this choice below in several cases. In all that follows, when considering a variation on some parameter, all others will be set to the default value from the table.

3.1. Cutoff Magnetic Field Strength (B_c)

Figure 2 shows how the L_X versus Φ_m relation changes as the value of cutoff magnetic field strength is increased. All cases are well fit by a broken power law, with a break at flux Φ^*, and indices $_{lo}$ and $_{hi}$ below and above it. As B_c is increased the break location decreases, and both indices decrease. For low values of B_c, $_{lo} > _{hi}$, creating a conventional "knee" (see Figures 2(a)–(c)). The index $_{lo}$ decreases more rapidly (see Figure 3), until, at a critical cutoff, B_c^*, the indices match to within fitting uncertainty, $|\alpha_{lo} - \alpha_{hi}| < \sqrt{\delta\alpha_{lo}^2 + \delta\alpha_{hi}^2}$ (see Figure 2(d)). At this point ($B_c = 45$ 8 G) the broken fit is equivalent to a single power-law index, $_0 = 1.280$ 0.043, or $L_X \sim \Phi_m^{1.280}$. For values $B_c > B_c^*$, $_{lo} < _{hi}$ and the "knee" structure inverts (see Figures 2(e)–(f)). The break point, Φ^*, jumps at $B_c = B_c^*$ but thereafter decreases as B_c increases.

Table 1
Default Value of Parameters Used in This Study

Parameter	Default Value
R_X	$0.83_\odot$
R_m	$0.79_\odot$
W_X	2.8–36.6 Å
CHIANTI version	10.0
Abundance model	Corona
XRT filter pair	Al-poly and Thin-Be
Time average	No averaging

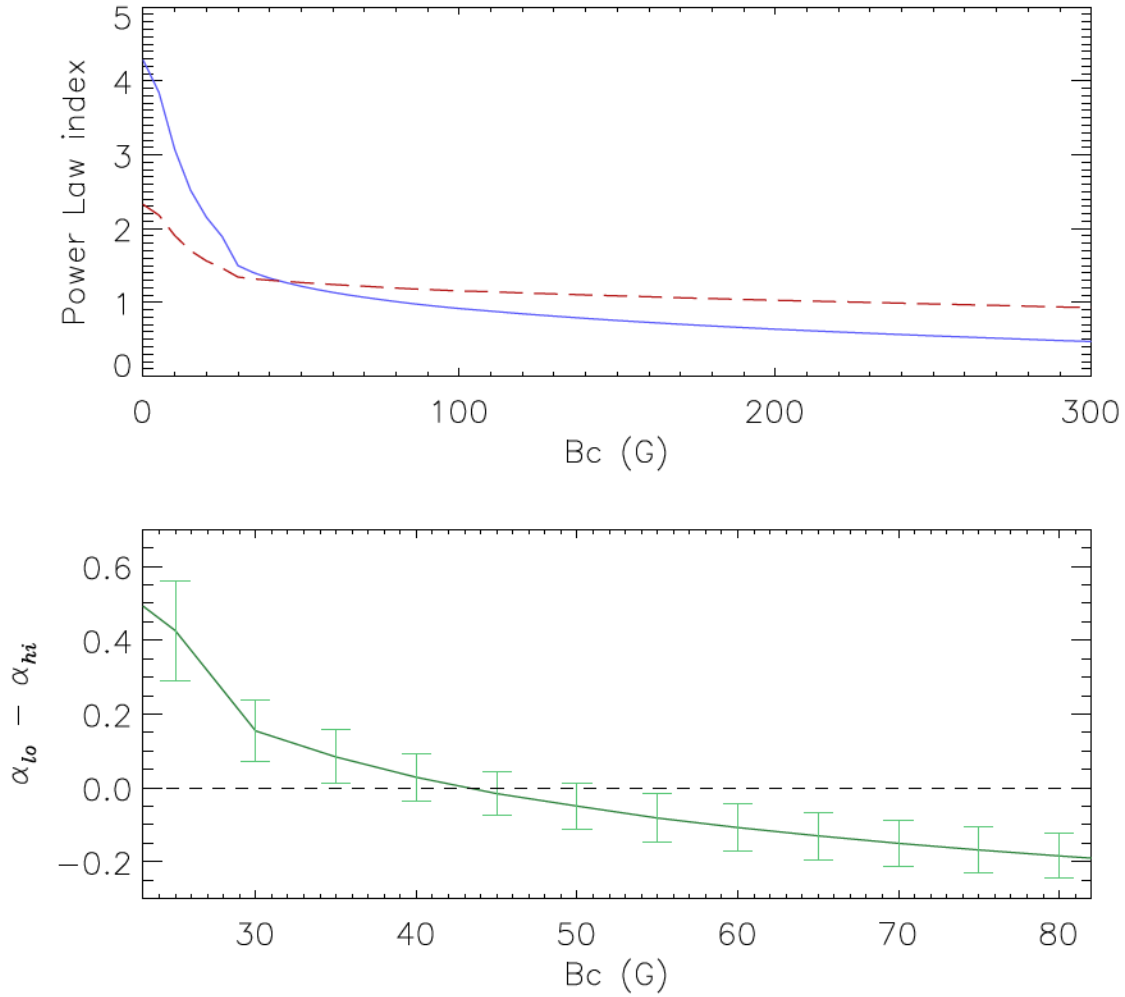

Figure 3. The change of the power-law indices of the lower ($_{\rm lo}$, blue) and the higher ($_{\rm hi}$, red dashed) part with respect to the B_c. The lower panel shows the differences $_{\rm lo} - _{\rm hi}$ (green) in the neighborhood of $B_c = 50$ G. Error bars show the uncertainty in the difference $\sqrt{\delta\alpha_{\rm lo}^2 + \delta\alpha_{\rm hi}^2}$.

When $B_c = B_c^*$, the rms fitting residual for a broken power law reaches a minimum of 0.046, where it is very nearly the same as that of a single power-law fit. For the cases above and below it, $B_c = 40$ and 80 G, the residual from a broken power law is only slightly greater than for a single power law. The minimum fitting residual in $\log_{10}(L_{\rm X})$ translates into 11% scatter, which is consistent with our estimate of the intrinsic variability of $L_{\rm X}$; the data cannot be fit better than this.

Similar behavior occurs as B_c is varied while other parameters set to values other than the defaults, as considered below. In each case there is a particular value, B_c^*, where the data are consistent with a single power law, and the fitting residual achieves its minimum. Below this value the data shows a conventional "knee" structure and above it an inverted knee. The value of B_c^* varies with choice of parameter. It is of note that in every case B_c^* far exceeds the quoted level of noise for HMI LOS magnetograms ($\simeq$6.3 G; Y. Liu et al. 2012).

3.2. Integration Radius (R_X and R_m)

Our guiding hypothesis is that photospheric footpoints counted in Φ_m contribute somehow to the formation of the hot corona quantified by $L_{\rm X}$. This process is expected to lead to the statistical relationship observed between the quantities. These structures lie some distance apart, so we expect their separation on the sky to somewhat obscure the statistical relationship. To explore this effect we vary radii $R_{\rm X}$ and R_m independently, and for each pair we compute the Pearson correlation coefficient

$$r = \frac{\sum_j x_j\, y_j}{\sqrt{\sum_j x_j^2}\,\sqrt{\sum_j y_j^2}}, \tag{2}$$

where

$$x_j = \log_{10}(L_{x,j}) - \frac{1}{N}\sum_{i=1}^{N}\log_{10}(L_{x,i}), \tag{3}$$

$$y_j = \log_{10}(\Phi_{m,j}) - \frac{1}{N}\sum_{i=1}^{N}\log_{10}(\Phi_{m,i}) \tag{4}$$

for each time j. In doing so we keep all other parameters at their default values and set $B_c = 45$ G, which is found to approximate B_c^* over the different values of $R_{\rm X}$ and R_m.

Figure 4 shows the value of r as color over the range of $R_{\rm X}$ and R_m explored. The tightest relationship ($r \simeq 1$) occurs slightly below the diagonal, where $R_{\rm X} = R_m$. The slight discrepancy may occur because the coronal structures are higher, and possibly broader, than the photospheric features

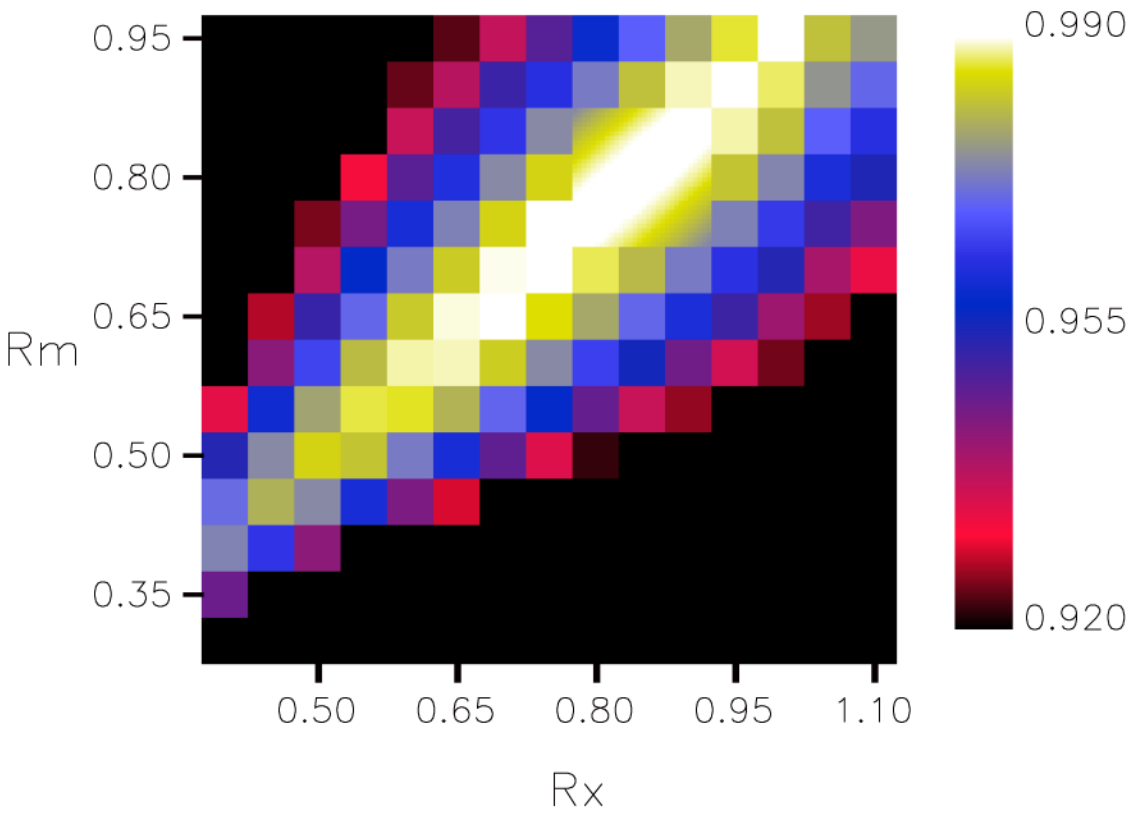

Figure 4. Map of cross-correlation coefficients between $\log_{10}(L_X)$ and $\log_{10}(\Phi_m)$ for selected R_X and R_m.

they anchor to. The correlation coefficient peaks at $R_X = 0.83\,R_\odot$ and $R_m = 0.79\,R_\odot$, which we therefore choose as default values.

3.3. Wavelength Range for X-Ray Integration (W_X)

The definition of X-ray luminosity L_X depends on the range of wavelengths over which synthesized emission is integrated. For example, including only short wavelengths in the integration will emphasize contributions from hotter coronae, which could affect the inferred scaling with magnetic flux. To understand this effect, we consider several different choices of W_X. We subdivide the default range into three equal bins and add a fourth bin at longer wavelengths, 36.0–60.0 Å, where XRT has sensitivity. Figure 5 shows the L_X–Φ_m scatter plots for different integral X-ray wavelength ranges. For the same B_c, the power-law indices are fairly large in the short-wavelength range, but they are close to unity at $B_c = B_c^*$, where the distribution conforms to a single power law. This critical cutoff is found to vary with W_X, decreasing at longer wavelengths. However, the single power-law indices obtained with B_c^* do not vary in the same manner but settle around the values close to 1.2. These behaviors are summarized in Table 2. We will discuss this further in Section 4.

3.4. Different Combination of XRT Filters

Figure 6 show the results from different XRT filter pairs, "Al-Mesh/Al-Poly" ((a), (b), (c)), "Al-Mesh/Thin-Be" ((d), (e), (f)), and "Al-Mesh/Al-Poly" ((g), (h), (i)). No major differences can be found. B_c^* is similar, at 55 8 G for "Al-Mesh/Al-Poly" (= 1.396 0.045) and 50 8 G for "Al-Mesh/Thin-Be" (= 1.164 0.044). The results from the Al-Mesh/Thin-Be combination show more dispersion than others. This may be attributed to the difference of the temperature responses between Al-Mesh and Thin-Be filters, which is the largest in all the combinations in this study. The power-law indices of the combination "Al-Mesh/Al-Poly" are slightly higher than the others.

3.5. CHIANTI and Coronal Abundance Model

The different CHIANTI versions (10.0 or 9.1) and coronal abundance models ("corona" or "hybrid") do not affect the results much. Since the luminosities calculated by CHIANTI 9.1 with "corona" abundance (L_{X1}) show the largest difference from the ones by 10.0 with "corona" (L_{X0}), we show the ratio L_{X1}/L_{X0} in Figure 7(a) as a function of L_{X0}, as an example. The ratio diverges to around 1.1 at the lower luminosity end, or the solar minimum period. In other words, during the solar minimum, the X-ray luminosity calculated by CHIANTI version 9.1 is overestimated by 10% in comparison to CHIANTI version 10.0.

Even in this case of the largest difference, no major changes can be found in the log–log scale plots (Figures 7(b) and (c)), which results in similar B_c^* (38 5 G) and (1.307 0.036).

3.6. Time Average

A. A. Pevtsov et al. (2003) used $R_X = 1.1R_\odot$ for their X-ray flux calculation. So, in their case, some of the coronal structures seen in the X-ray images are not connected to the on-disk photospheric magnetic field. In order to mitigate the discrepancy, they applied solar rotation averages to magnetic and X-ray fluxes. Since we do not count the X-ray fluxes above the limb with $R_X = 0.83R_\odot$, we have no need for such

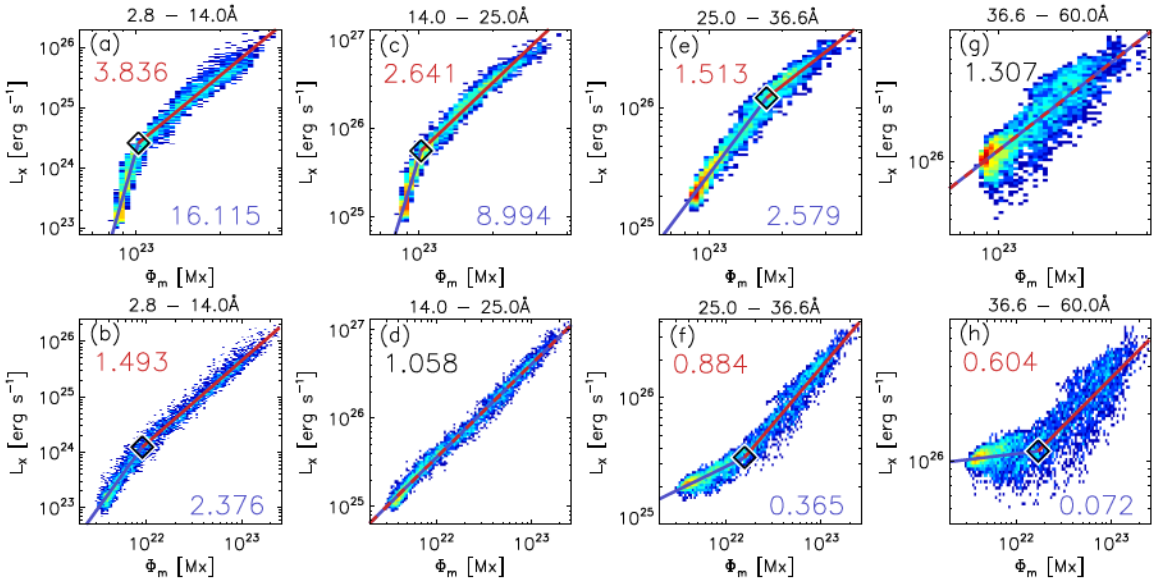

Figure 5. L_X–Φ_m distributions with different W_X, 2.8–14.0 ((a), (b)), 14.0–25.0 ((c), (d)), 25.0–36.6 ((e), (f)), and 36.6–60.0 Å ((g), (h)). B_c is 0 G for the upper row and 150 G for the lower row.

Table 2
The Critical Cutoff Field Strength (B_c^*) and the Power-law Index ( ) for Each Wavelength Range (W_X) for X-Ray Integration

W_X (Å)	B_c^* (G)		Power-law Index	
2.8–14.0	325	10	1.241	0.021
14.0–25.0	130	15	1.106	0.035
25.0–36.6	18	3	1.261	0.012
36.6–60	<5		1.305	0.039
2.8–36.6	45	8	1.280	0.043

an averaging process. However, in this subsection, we show the results through different time averages just for comparison.

Figure 8 shows the results from the different time average of the data (1, 5, 14, and 27 days). The application of time averaging has the effect of reducing the dispersion to a very limited extent and does not appear to be an effective approach to reduce the noise.

4. Discussion

We have reproduced, using more recent data sets, the scaling of solar X-ray luminosity, L_X, with the Sun's full-disk unsigned magnetic flux, Φ_m, previously reported by A. A. Pevtsov et al. (2003). We find a scaling with similar power, near $L_X \sim \Phi_m^{1.2}$, although the exponent is found to depend on the choice of certain parameters. We also manage to reproduce the broken power law, featuring a "knee" at around Φ_m 10^{23} Mx, when Φ_m is computed without a field-strength cutoff: $B_c = 0$. Indeed, the knee persists, albeit at a different flux, when the field measurements are cut off safely above the expected noise level, ≃6.3 G.

The dependence of scaling on cutoff field, B_c, points to a complexity in the relationship between X-ray luminosity and full-disk unsigned magnetic flux. Increasing B_c from zero causes the knee to move leftward (toward lower fluxes) and for the disparate power laws to flatten and converge toward one another (see Figure 3). At a critical value, B_c^*, the two powers coincide, yielding a single power law relating the X-ray luminosity to unsigned magnetic flux over the entire range. The index of this single relation is close to the value reported by A. A. Pevtsov et al. (2003) for fluxes of all kinds—not only the full solar disk. The cutoff value B_c^* is also optimal in the sense that the L_X–Φ_m relation is fit, by either a single or broken power law, with a lower residual than for other cutoff choices.

If one conjectures that such a single power law, lacking a characteristic global flux of Φ^* 10^{23} Mx, actually governs the generation of the global X-ray corona, then the particular cutoff value, B_c^*, might be required in order to measure only that flux directly related to the hot corona. Under this hypothesis, including weaker field increases Φ_m by adding flux that does not contribute to L_X. This slides the leftmost points rightward, steepening the L_X–Φ_m relation for smaller values, thereby creating an artificial "knee."

Such an effect certainly compromises the case with no cutoff: $B_c = 0$. Magnetic field measurement of intrinsically weak pixels will be dominated by Gaussian noise, whose mean magnitude is $\sqrt{2/\pi}$ times the noise level (≃5.0 G for HMI). Including projection effects out to $R_m = 0.79\,R_\odot$, a perfectly field-free Sun would register a flux of $\Phi_m = 7.5 \times 10^{22}$ Mx due to noise alone. Using the cutoff value of $B_c = 20$ G, four times the level contributed by noise, should eliminate these spurious pixels entirely. The difference, $\Delta\Phi_m$, between Φ_m measured with $B_c = 0$ and $B_c = 20$ G, shown in Figure 9(a), is divided into groups, depending on the date when the original level 1.5 HMI data was created. The data of the upper group (median 6.33×10^{22} Mx) were created before 2016 April 18 and the lower (median 5.79×10^{22} Mx) after that date. The two groups are distributed very narrowly about each median, with very little relation to the latter flux, at least out to $\Phi_m \simeq 1.5 \times 10^{23}$ Mx. This strongly suggests that including fields $|B_r| < 20$ G contributes an additive constant to the unsigned flux under all conditions.

An additive bias in the case with $B_c = 0$ may help explain why the distribution in Figure 2(a) curves downward fairly smoothly. This smooth downward curve is fit rather poorly by a broken power law, with an rms residual of 0.075, while all

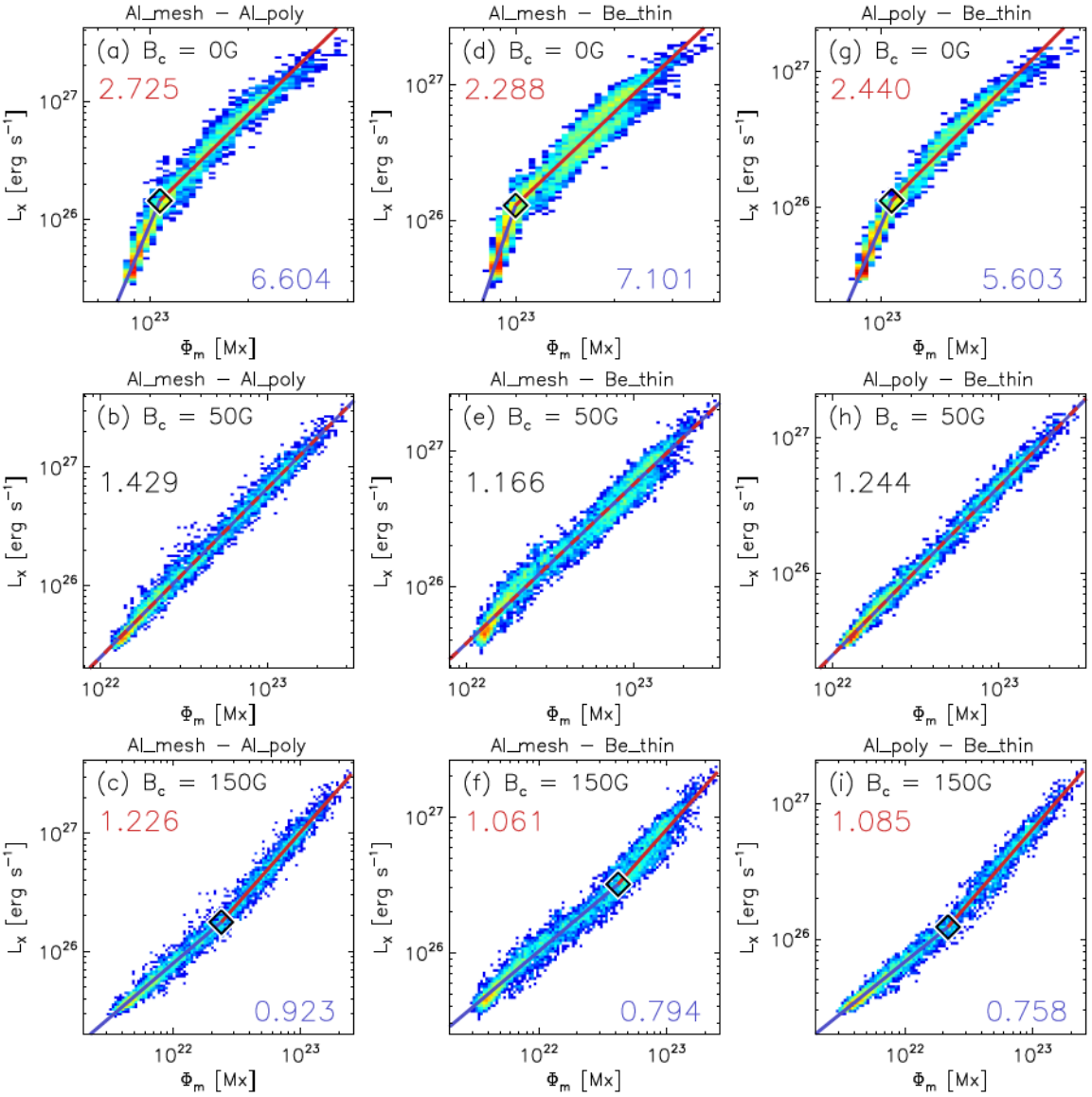

Figure 6. L_X–Φ_m distributions with different XRT filter pairs, Al-Mesh + Al-Poly ((a), (b), (c)), Al-Mesh + Thin-Be ((d), (e), (f)), and Al-Poly + Thin-Be ((g), (h), (i)). B_c is 0 G for the top row, 50 G for the middle, and 150 G for the bottom.

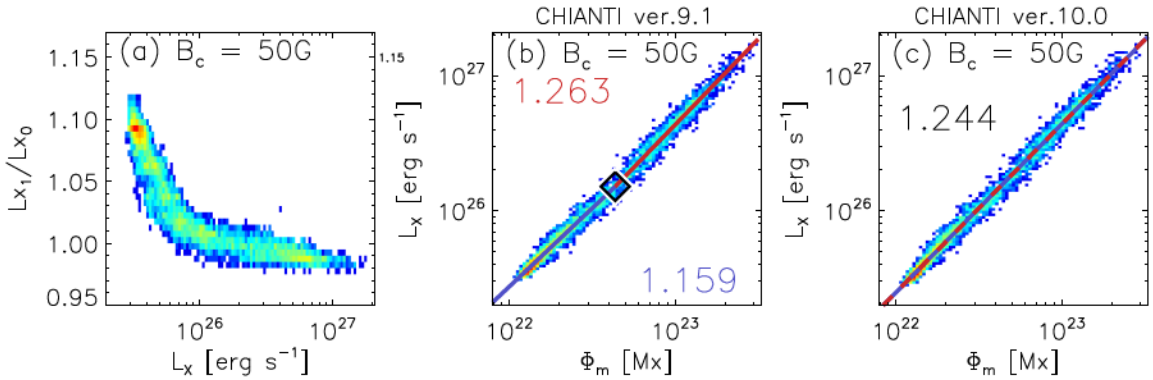

Figure 7. L_X–Φ_m distributions with different CHIANTI versions, version 9.01 (b) and 10.0 (c). The ratio of the two results is plotted in (a).

other cases are below 0.06. Making the simple correction of subtracting the fixed values, $\Phi_0 = 6.33 \times 10^{22}$ (for the data before 2016 April 18) and 5.8×10^{22} Mx (for the data after 2016 April 18), from each no-cutoff measurement, Φ_m, produces a straighter distribution, capable of fitting a single power law (see Figure 9(b)) but with virtually the same residual (0.074 rms). Subtracting different pairs of offsets produces larger residuals.

This procedure is similar to the approach of S. Toriumi & V. S. Airapetian (2022) who analyzed power-law relationships

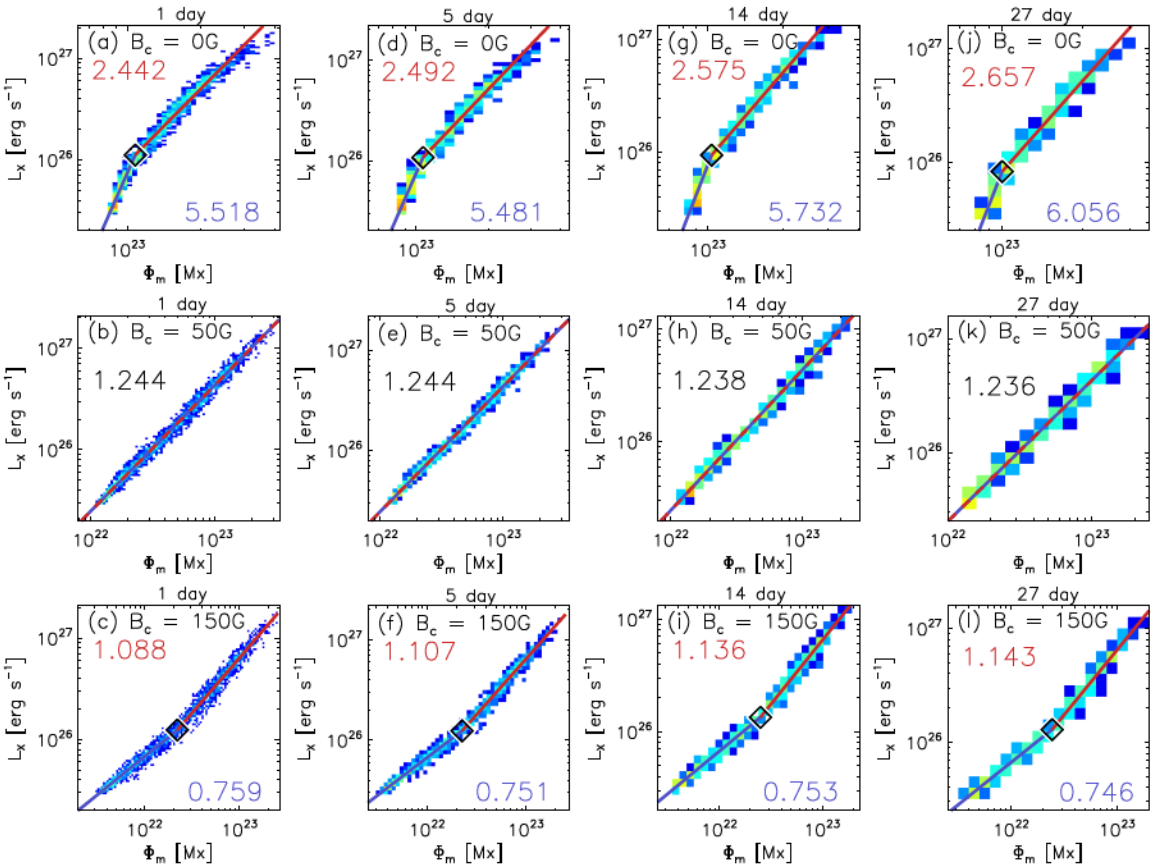

Figure 8. L_X–Φ_m distributions with different time average spans, 1 ((a), (b), (c)), 5 ((d), (e), (f)), 14 ((g), (h), (i)), and 27 days ((j), (k), (l)). B_c is 0 G for the top row, 50 G for the middle, and 150 G for the bottom.

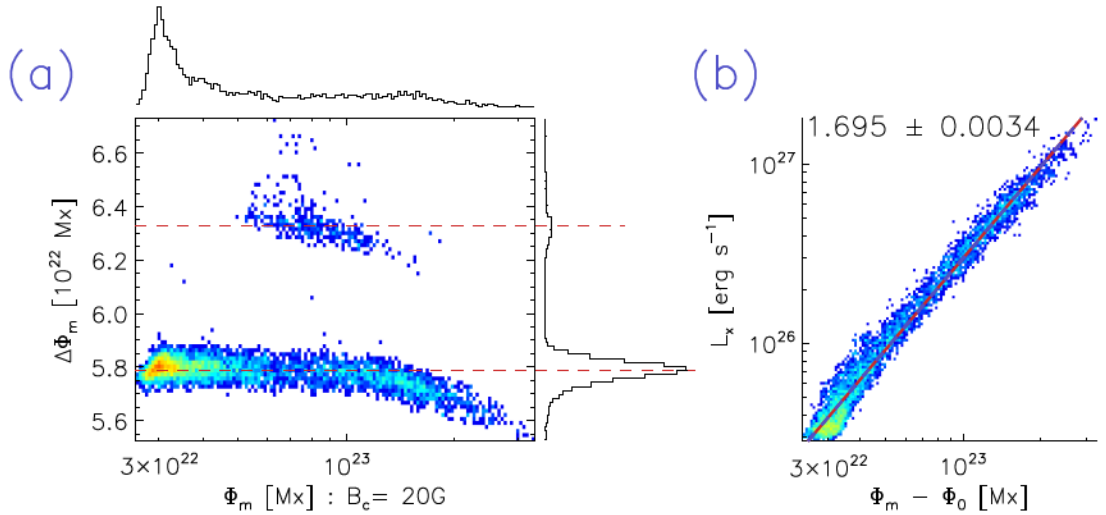

Figure 9. The effects of weak pixels on the $B_c = 0$ G measurements. (a) A two-dimensional histogram of $\Delta\Phi_m$, the difference between Φ_m measured with $B_c = 0$ and $B_c = 20$ G vs. the latter flux. The magenta dashed lines are the medians of two populations, $\Phi_0 = 5.79 \times 10^{22}$ and 6.33×10^{22} Mx. One-dimensional histograms are plotted along the top and the right. (b) The relationship between L_X and $\Phi_m - \Phi_0$, for the case with $B_c = 0$ G. A single power-law fit is shown by the blue–red line.

after subtracting a basal flux from the full-disk integral of unsigned flux computed with $B_c = 0$. They computed the basal flux $\Phi_0 \simeq 1.18 \times 10^{23}$ Mx from the median of low values found over their 9 yr data set. Their value is about twice ours, presumably due to several factors. They integrate over the entire hemisphere rather than a restricted disk. Their sets of low values all include quiet Sun, which is weak but not equivalent to zero.

The notable improvement of fitting achieved by selecting the cutoff values well above the noise level (i.e., $B_c \gg 6.3$ G) suggests the existence of a weak but measurable photospheric magnetic field that anchors flux not contributing to X-ray luminosity. To explore this further, we analyze sample data representing active, quiet, and coronal hole regions, shown in Figure 10. The red pixels in the top row of images show the locations of the weak magnetic field whose strength

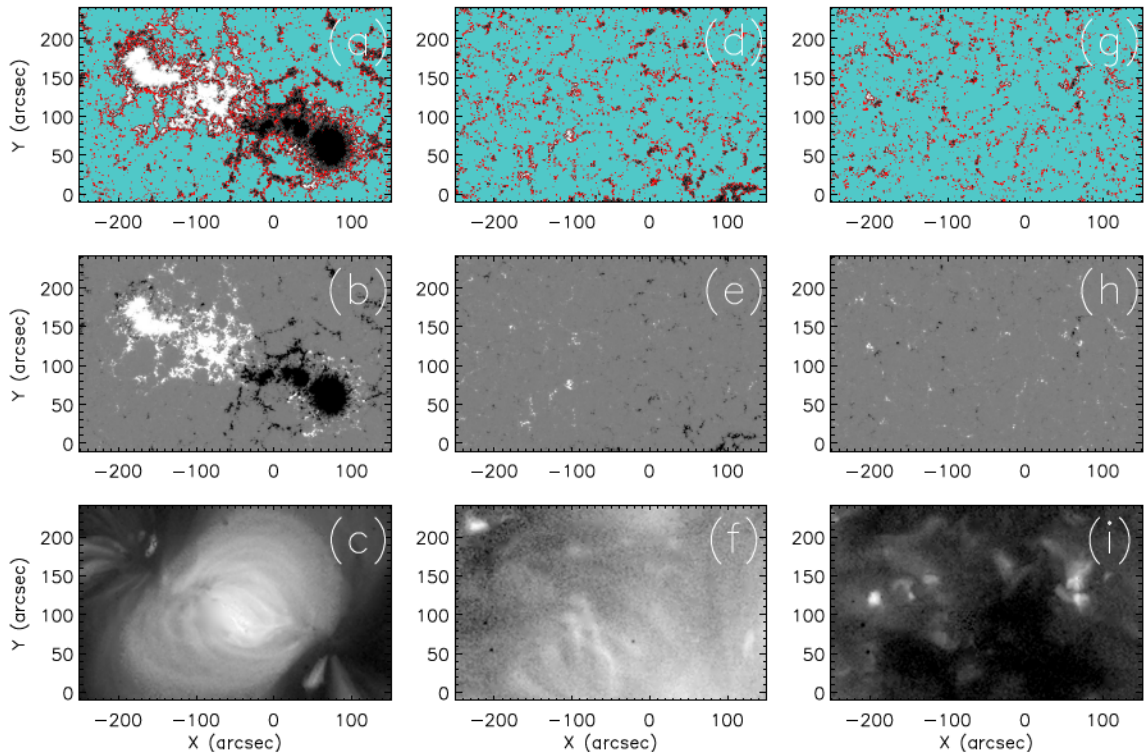

Figure 10. HMI magnetogram samples of an active region (left column), a quiet region (middle), and a coronal hole (right). The XRT Al-poly images corresponding to the magnetograms are in the bottom row. The red pixels in (a), (d), and (g) are where the magnetic field strengths are stronger than the noise (3σ level, 18.9 G) and weaker than 50 G. The cyan pixels are where the magnetic field strengths are weaker than the noise level.

is larger than the noise level ($3\sigma = 18.9$ G) but smaller than $B_c^* = 50$ G. While most of them are found in the surrounding area of strong magnetic concentrations, they are also found in super granular network boundaries. Table 3 shows that the weak magnetic field covers about 10% of the total area and constitutes 4% of total unsigned magnetic flux in the sample active region. On the other hand, it covers 4%–5% of the total area and accounts for about 17% of total flux in the sample regions of quiet region and coronal hole. Our study shows that such weak magnetic fields in addition to those under the noise level do not contribute significantly to the X-ray luminosity because the best single power law between L_X versus Φ_m is obtained by eliminating those components. In the sample regions of quiet Sun and a coronal hole, these components take more than 97% of area and roughly 70% of total unsigned magnetic field.

By adopting the critical cutoff B_c^* we believe we uncover the fundamental relationship underlying coronal heating: $L_X \sim \Phi_m^{1.2}$. Subsets of data restricted to solar minimum, solar maximum, and the rising and declining phases of solar cycles show equivalent relations and require the same value of $B_c^* = 50$ G.

We also found smaller power-law indices in longer X-ray wavelength range (W_X) for the same cutoff B_c (Figure 5). This reflects the amplitude of luminosity over a solar cycle calculated at the specified wavelength range. In the 2.8–14.0 Å range, $\log_{10}(L_X)$ roughly varies from 23.0 to 26.2 over solar cycle, while the variation is 25.0–26.4 in 25.0–36.6 Å range. On the other hand, the subtraction of B_c generally works to reduce the range of magnetic field. By subtracting a specific value of B_c^* for each wavelength range, the effect of L_X variation over solar cycle is mitigated to result in the relatively uniform values of power-law indices shown in Table 2. S. Toriumi & V. S. Airapetian (2022) reported the same trend with data of much wider wavelength range. They attributed the trend to the efficiency of the plasma heating. While they measured luminosity from plasma of different temperature, we use only X-ray data with the assumption of single plasma temperature. Our results may suggest the trend can be explained by a property of emission, not by a different EM of different plasma temperature.

It is important to note that the power-law indices derived from various parameters show considerable variation. However, these indices approach unity when the distributions can be characterized by a single power law.

Table 3
Total Unsigned Magnetic Flux Included in Three Ranges: Noise Level ($B < 18.9$ G, Cyan in Figure 10), Weak ($18.9 < B < 50$ G, Red in Figure 10), and Strong ($B > 50$ G)

	$B < 19$ G	19 G $< B <$ 50 G	$B > 50$ G
⟨Active Region			
Area (%)	70.8	9.8	19.4
Magnetic Flux (Mx)	1.89×10^{21}	1.65×10^{21}	36.31×10^{21}
Magnetic Flux (%)	4.7	4.1	91.1
⟨Quiet Region			
Area (%)	92.8	4.9	2.4
Magnetic Flux (Mx)	2.20×10^{21}	0.75×10^{21}	1.58×10^{21}
Magnetic Flux (%)	48.6	16.5	34.9
⟨Coronal Hole			
Area (%)	94.5	4.0	1.4
Magnetic Flux (Mx)	2.05×10^{21}	0.60×10^{21}	0.84×10^{21}
Magnetic Flux (%)	58.8	17.2	24.0

Note. Their fractions relative to those of the whole sampled region, as well as their areal fraction, are shown.

The study of the relationship L_X and Φ_m in this paper uses only the disk-integrated value. We will extend our research to each part of the Sun, such as active regions, X-ray bright points, and quiet regions, in our future study.

Acknowledgments

Hinode is a Japanese mission developed and launched by ISAS/JAXA, with NAOJ as domestic partner and NASA and STFC (UK) as international partners. It is operated by these agencies in cooperation with ESA and NSC (Norway). The HMI data are courtesy of NASA/SDO and the HMI science team. HMI is an instrument on board SDO, a mission for NASA's Living With a Star program. CHIANTI is a collaborative project involving George Mason University, the University of Michigan (USA), University of Cambridge (UK), and NASA Goddard Space Flight Center (USA). K.Y. and A.T. are supported by NASA under contract NNM07AB07C with the Smithsonian Astrophysical Observatory.

ORCID iDs

Keiji Yoshimura https://orcid.org/0000-0001-8258-609X

References

Couvidat, S., Schou, J., Hoeksema, J. T., et al. 2016, SoPh, 291, 1887
Del Zanna, G., Dere, K. P., Young, P. R., & Landi, E. 2021, ApJ, 909, 38
Dere, K. P., Del Zanna, G., Young, P. R., Landi, E., & Sutherland, R. S. 2019, ApJS, 241, 22
Dere, K. P., Landi, E., Mason, H. E., Monsignori Fossi, B. C., & Young, P. R. 1997, A&AS, 125, 149
Edlén, B. 1943, ZA, 22, 30
Feldman, U. 1992, PhyS, 46, 202
Fisher, G. H., Longcope, D. W., Metcalf, T. R., & Pevtsov, A. A. 1998, ApJ, 508, 885
Fludra, A., & Schmelz, J. T. 1999, A&A, 348, 286
Golub, L., Deluca, E., Austin, G., et al. 2007, SoPh, 243, 63
Golub, L., Maxson, C., Rosner, R., Vaiana, G. S., & Serio, S. 1980, ApJ, 238, 343
Grotrian, W. 1939, NW, 27, 214
Kano, R., Sakao, T., Hara, H., et al. 2008, SoPh, 249, 263
Klimchuk, J. A. 2006, SoPh, 234, 41
Klimchuk, J. A. 2015, RSPTA, 373, 20140256
Kobelski, A. R., Saar, S. H., Weber, M. A., McKenzie, D. E., & Reeves, K. K. 2014, SoPh, 289, 2781
Kochukhov, O., Hackman, T., Lehtinen, J. J., & Wehrhahn, A. 2020, A&A, 635, A142
Kosugi, T., Matsuzaki, K., Sakao, T., et al. 2007, SoPh, 243, 3
Liu, Y., Hoeksema, J. T., Scherrer, P. H., et al. 2012, SoPh, 279, 295
Narukage, N., Sakao, T., Kano, R., et al. 2011, SoPh, 269, 169
Parnell, C. E., & De Moortel, I. 2012, RSPTA, 370, 3217
Pevtsov, A. A., Fisher, G. H., Acton, L. W., et al. 2003, ApJ, 598, 1387
Press, W. H., Teukolsky, S. A., Vetterling, W. T., & Flannery, B. P. 1992, Numerical Recipes: The Art of Scientific Computing (2nd ed.; Cambridge: Cambridge Univ. Press)
Reale, F. 2010, LRSP, 7, 5
Scherrer, P. H., Schou, J., Bush, R. I., et al. 2012, SoPh, 275, 207
Schou, J., Scherrer, P. H., Bush, R. I., et al. 2012, SoPh, 275, 229
Shoda, M., & Takasao, S. 2021, A&A, 656, A111
Takeda, A., Yoshimura, K., & Saar, S. H. 2016, SoPh, 291, 317
Toriumi, S., & Airapetian, V. S. 2022, ApJ, 927, 179
Vaiana, G. S., Krieger, A. S., & Timothy, A. F. 1973, SoPh, 32, 81
Vidotto, A. A., Gregory, S. G., Jardine, M., et al. 2014, MNRAS, 441, 2361
Yashiro, S., & Shibata, K. 2001, ApJL, 550, L113